Journal of Alloys and Compounds 509 (2011) 1138–1145

Contents lists available at ScienceDirect

Journal of Alloys and Compounds

journal homepage: www.elsevier.com/locate/jallcom

# Electrical conductivity studies of nanocrystalline lanthanum silicate synthesized by sol–gel route

N. Nallamuthu [a], I. Prakash [a], N. Satyanarayana [a,*], M. Venkateswarlu [b]

[a] Department of Physics, Pondicherry University, Puducherry 605 014, India
[b] R & D, Amara Raja Batteries Ltd., Tirupati 517520, AP, India

ARTICLE INFO

*Article history:*
Received 4 March 2010
Received in revised form
21 September 2010
Accepted 26 September 2010
Available online 7 October 2010

*Keywords:*
Nanostructured materials
Sol–gel process
TG/DTA
XRD
FTIR
SEM-EDX
Impedance spectroscopy
Ionic conduction
Dielectric relaxation

ABSTRACT

Nanocrystalline apatite type structured lanthanum silicate ($La_{10}Si_6O_{27}$) sample was synthesized by sol–gel process. Thermal behavior of the dried gel of lanthanum silicate sample was studied using TG/DTA. The structural coordination of the dried gel of lanthanum silicate, calcined at various temperatures, was identified from the observed FTIR spectral results. The observed XRD patterns of the calcined dried gel were compared with the ICDD data and confirmed the formation of crystalline lanthanum silicate phase. The average crystalline size of $La_{10}Si_6O_{27}$ was calculated using the Scherrer formula and it is found to be ~80 nm. The observed SEM images of the lanthanum silicate indicate the formation of the spherical particles and the existence of O, Si and La in the lanthanum silicate are confirmed from the SEM-EDX spectrum. The grain and grain boundary conductivities are evaluated by analyzing the measured impedance data, using winfit software, obtained at different temperatures, of $La_{10}Si_6O_{27}$ sample. Also, the observed grain and grain boundary conductivity behaviors of the $La_{10}Si_6O_{27}$ sample are analysed using brick layer model. The electrical permittivity and electrical modulus were calculated from the measured impedance data and were analyzed by fitting through the Havriliak and Negami function to describe the dielectric relaxation behavior of the nanocrystalline lanthanum silicate.



## 1. Introduction

Solid oxide fuel cells have considerable interest in the recent years because of the pollution free generation of electricity at higher efficiencies through electrochemical reactions as well as fuel adaptability and low level emission of $NO_x$ and $SO_x$ gases [1–3]. Solid oxide fuel cell system usually uses ceramic oxides like $ZrO_2$, $ThO_2$, $HfO_2$, $CeO_2$, etc., as electrolytes, working above 1000 °C [4]. In order to avoid the problem related to the thermal stability of solid electrolytes at high temperatures, researchers are motivated to prepare high conducting electrolyte materials for solid oxide fuel cell applications and can be operated relatively at intermediate temperatures between 500 and 800 °C. To enhance the oxygen ion conductivity of the solid electrolytes at lower temperatures, researchers are trying to develop some new oxygen ion conductors such as $LaGaO_3$, $La_2Mo_2O_9$ based on perovskites, brownmillerite (e.g., derived from $Ba_2In_2O_5$), several new pyrochlores, etc. [5]. Recent investigations reported that apatite type lanthanum silicate materials are having conductivities higher than yttrium-stabilized zirconia at intermediate temperatures. In general, apatite type materials are having many applications including luminescent, nuclear waste management, biomaterials and also potential use as solid electrolytes [6]. On the other hand, wide variety of apatite type crystalline $La_{9.33}(SiO_4)_6O_2$ materials exist as a cation deficient structure and $La_{10}Si_6O_{27}$ exist as an interstitial anion structure provide high ionic conductivity. The apatite type lanthanum silicate $[La_{9.33}(SiO_4)_6O_2]$ consists of isolated $SiO_4$ tetrahedra, large number of $La^{3+}$ cations located in two sites (one 7-coordinated and another 9-coordinated) and $O_2$ anions occupying the channels along the *c*-axis [7]. The insertion of excess $La_2O_3$ into $La_{9.33}(SiO_4)_6O_2$ can be expressed as:

$$La_{9.33}\square_{0.67}(SiO_4)_6O_2 + (1/3)La_2O_3 = La_{10}(SiO_4)_6O_2O_i\,[La_{10}(SiO_4)_6O_3] \quad (1)$$

An extra interstitial oxygen is introduced into the lattice of $La_{10}(SiO_4)_6O_3$, in which the 4f and 6h sites are fully occupied by $La^{3+}$ ions. In the apatite type rare earth based metal oxides, interstitial oxygen structured $La_{10}(SiO_4)_6O_3$ exhibits higher conductivity than the cation deficient structured $La_{9.33}(SiO_4)_6O_2$.

Nanocrystalline materials exhibit novel properties due to nanoconfinement compared to their respective bulk. Nanocrystalline electrolyte materials having small grains, which increase

* Corresponding author. Tel.: +91 413 2654404; fax: +91 413 2655260/11.
*E-mail addresses:* nallanis2000@yahoo.com, ionics2003@yahoo.co.in (N. Satyanarayana).

0925-8388/$ – see front matter © 2010 Elsevier B.V. All rights reserved.
doi:10.1016/j.jallcom.2010.09.141

the grain boundary area and showed improved conductivity, since grain boundaries have more interstitials space to transport the oxygen ions [8]. Preparation of rare earth based metal oxide powders using wide range of solid state reaction methods involve the heating of precursor materials at higher temperature, result in inhomogeneity, bigger crystallite size and poor stoichiometry. These problems could be avoided using low temperature wet chemical methods, such as co-precipitation, sol–gel, hydrothermal, gel combustion, etc. Among the available process, sol–gel process is found to be the most versatile technique to prepare nanocrystalline materials because of its advantages to prepare highly homogenous, better stoichiometric and high pure materials at low temperature [9–12]. Hence, our interest is oriented towards the preparation of nanocrystalline $La_{10}Si_6O_{27}$ by sol–gel process, its structural characterization using XRD, FTIR, TG/DTA and SEM-EDX techniques and ionic transport studies like, conductivity and the relaxation behavior through impedance measurements to develop the better property solid electrolyte for intermediate temperature solid oxide fuel cell applications.

## 2. Experimental

### 2.1. Sol–gel process

The precursor chemicals tetraethylorthosilicate (TEOS) (Aldrich), lanthanum nitrate (SRL), ethylalcohol and distilled water were used for the synthesis of lanthanum silicate by sol–gel process. All the chemicals were mixed according to their molecular weight percentage of $La_{10}Si_6O_{27}$ by following the given procedure. Initially, the lanthanum nitrate solution was prepared by dissolving the required amount of lanthanum nitrate in the distilled water. The stoichiometric amount of TEOS, ethanol and water were mixed in 100 ml beaker on continuous stirring. The molar ratio of TEOS and water was kept as 1:16 and the ethyl alcohol and TEOS were mixed with equal volume ratio. 2.5 N nitric acid was added as catalyst to the above solution on continuous stirring. The resultant clear transparent solution was added to the lanthanum nitrate solution and stirred at an ambient temperature for 2 h to get clear transparent solution. The formed clear solution, called sol, was kept in a dry atmosphere to form the gel. The gel formation was clearly noticed by its viscous nature and clear transparent monolithic gel was obtained. The dried gel was heated at higher temperatures to obtain the nanocrystalline lanthanum silicate and it was characterized using TG/DTA, FTIR, XRD and SEM-EDX techniques.

### 2.2. Measurement techniques

The TG/DTA curve for the dried gel sample of $La_{10}Si_6O_{27}$ was recorded using TA instrument of SDT Q600 V20.5 DTA-TGA thermal analyzer at the heating rate of 10 °C/min between 30 °C and 1200 °C in nitrogen atmosphere. Thin transparent pellet samples were prepared using the dried gel samples, obtained at 100 °C and 600–800 °C, grounded well with spectra pure KBr powder taken in 1:20 ratio. Fourier transform infrared spectra were recorded for the thin transparent pellet samples of $La_{10}Si_6O_{27}$ using Thermo Nicolet FTIR-6700 spectrometer in the frequency range of 4000–400 $cm^{-1}$ for 32 scans. Powder XRD patterns were recorded for the dried gel samples of $La_{10}Si_6O_{27}$, obtained at 100 °C and 600–800 °C, using X'Pert PRO MPD, PANalytical (Philips) X-ray powder diffractometer employing Cu-Kα radiation. The average crystallite size of the lanthanum silicate was calculated using Scherrer's formula. The sample was prepared by spreading the fine powdered lanthanum silicate and also the broken sintered lanthanum silicate pellet on the conducting carbon tape pasted over the aluminum stubs. Later, all of the samples were coated with a thin layer of gold using sputter coater for taking SEM images. For all the samples, SEM images and EDX spectra were taken using scanning electron microscope (SEM) (Hitachi-450 model). The $La_{10}Si_6O_{27}$ pellets sintered at 800 °C, with 10 mm diameter and 2–2.5 mm thickness were made under a pressure of 5 tons using spectralab make pelletizer. Silver paste as electrodes was painted on both side of each sintered lanthanum silicate pellet and heated at 200 °C for half an hour to ensure maximum contact and adherence. The real ($Z'$) and imaginary ($Z''$) parts of the impedance data were measured for the pellets using Novocontrol Alpha A High performance frequency analyzer in the frequency range 0.1 Hz to 1 MHz at different temperature. The measured impedance data were analyzed using the Win fit software to obtain bulk resistance and also its electrical behavior in terms of equivalent circuits. Also, the conductivity of nanocrystalline $La_{10}Si_6O_{27}$ sample was calculated using pellet dimension and bulk resistance obtained from the analysis of the measured impedance data at different temperature. Activation energy was calculated from the temperature dependence of conductivity plot of the nanocrystalline $La_{10}Si_6O_{27}$ sample.

Complex impedance ($Z^*$) data can be represented by its real ($Z'$) and imaginary ($Z''$) parts by the relation:

$$Z^* = Z' - iZ'' \tag{2}$$

The relations between the dielectric constant $\varepsilon'$, dielectric loss $\varepsilon''$, the real electric modulus $M'$ and the imaginary electric modulus $M''$ are given in the following equations [13],

$$M' = -\omega C_0 Z'' \tag{3}$$

$$M'' = \omega C_0 Z' \tag{4}$$

$$\varepsilon' = \frac{M'}{M'^2 + M''^2} \tag{5}$$

$$\varepsilon'' = \frac{M''}{M'^2 + M''^2} \tag{6}$$

where $C_0 = \varepsilon_0 A/t$ and $\varepsilon_0$ is the permittivity of the free space, $A$ and $t$ are area and thickness of the sample pellet. $\omega = 2\pi f$ ($\omega$ is the angular frequency in Hz).

The frequency dependence of the complex permittivity $\varepsilon^*$ in the case of a single relaxation (Debye type) dispersion is given by:

$$\varepsilon^* = \varepsilon_\infty + \left[\left((\varepsilon_s - \varepsilon_\infty)\frac{1}{1 + j\omega\tau}\right)\right] \tag{7}$$

where $\varepsilon_\infty$ and $\varepsilon_s$ are the limiting values of $\varepsilon^*$, respectively when $\omega$ is going towards $\infty$ and 0, $\tau$ is known as the dielectric relaxation time and it is the measure of the nominal time scale on which ion jump can take place. The above equation is not suitable for the system consists of many dielectric relaxations present and it could be taken in the form of cole relaxation function.

$$\varepsilon^* = \varepsilon_\infty + (\varepsilon_s - \varepsilon_\infty)\left(\frac{1}{(1 + j\omega\tau)^{1-n}}\right) \tag{8}$$

where $n$ may assume the values between 0 and 1.

Or more generally, the above equation can be written in the form of the empirical function introduced by Havriliak and Negami:

$$\varepsilon^* = \varepsilon_\infty + (\varepsilon_s - \varepsilon_\infty)\left[\left(\frac{1}{(1 + j\omega\tau)^{1-n}}\right)\right]^{1-\beta} \tag{9}$$

The exponents in the equation may assume the values such that $0 \le n$, $\beta \le 1$, $0 \le (1-\beta)(1-n) \le 1$ [14,15].

## 3. Results and discussion

### 3.1. TG/DTA

Fig. 1 shows the TG/DTA curve for $La_{10}Si_6O_{27}$ crystalline sample. From Fig. 1, the observed DTA endothermic peaks between 45 and 300 °C and the corresponding weight loss of 26.5% in TG curve and between 300 and 700 °C and the corresponding weight loss of 34.8% in TG curve are respectively attributed to the evaporation of water molecules and decomposition of organic compounds present in the sample. The total weight loss of 61.3% is observed between 45 °C and 700 °C and no other significant weight loss is observed above 700 °C, which confirmed that there is no further decomposition occurs in the sample after 700 °C and hence, the sample may be free from impurities, which is also confirmed from the FTIR results.

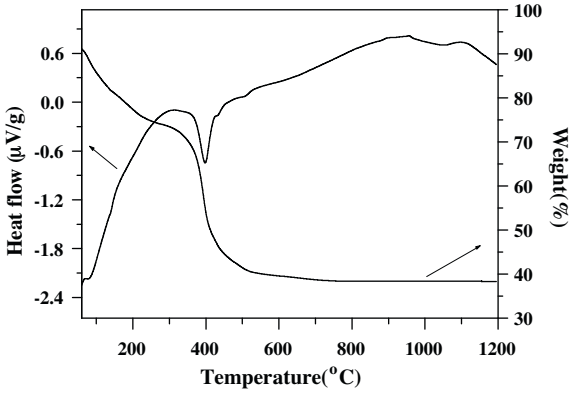


**Fig. 1.** TG/DTA curve of $La_{10}Si_6O_{27}$ dried gel sample.

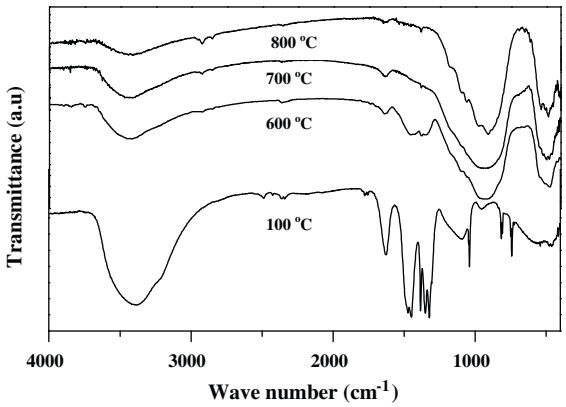


**Fig. 2.** FTIR spectra of $La_{10}Si_6O_{27}$ dried gel sample calcined at various temperatures.

### 3.2. FTIR

Fig. 2 shows the FTIR spectra for the dried gel of $La_{10}Si_6O_{27}$ sample, calcined at various temperatures (at 100 °C and 600–800 °C). From Fig. 2, the observed broad bands in the regions of 3395 and 1631 $cm^{-1}$ are attributed respectively to stretching and bending vibrational modes of O–H of molecular water and the Si–OH stretching of surface silanol hydrogen bond to molecular water. The bands at 1045, 1330 and 1458 $cm^{-1}$ are assigned to the organic residuals present in the sample, which are decomposed at higher temperature and it is confirmed from the disappearance of the corresponding IR bands on heating the sample. At 600 °C, the appearance of the IR band at 950 $cm^{-1}$ is due to formation of the ring structure of $SiO_4$ tetrahedral network and it became a sharp intense band at 800 °C [16]. The band at 467 $cm^{-1}$ is assigned to the formation of Si–O–Si and Si–O bonds [16]. The band observed at 640 $cm^{-1}$ is assigned to La–O network formation [17]. The observed IR bands corresponding to the absorbed water molecules, presence of organic residuals and their removal on heating are also reflected in the TG/DTA results.

### 3.3. X-ray diffraction

Fig. 3 shows the XRD patterns of the dried gel sample, heated at various temperatures. The dried gel sample, calcined at 600 °C showed the peak free XRD pattern and confirms the amorphous phase. Further heat treatment at 700 °C, resulted in the formation of peaks in the X-ray diffraction pattern. The observed XRD peaks were compared with ICDD (#053-0291) standard data and confirmed the formation of pure crystalline apatite $La_{10}Si_6O_{27}$ phase.

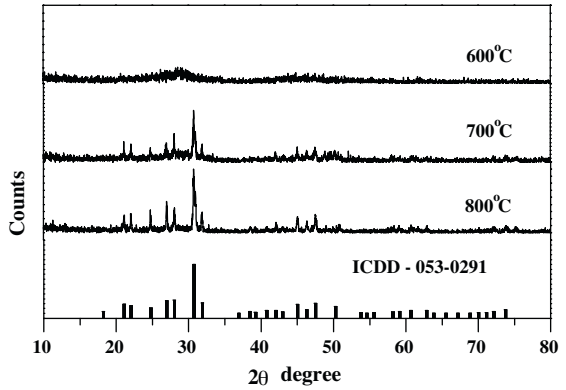


**Fig. 3.** XRD patterns along with JCPDS data of $La_{10}Si_6O_{27}$ dried gel sample calcined at various temperatures.

**Table 1**
Percentage of each element (La, Si, O) of lanthanum silicate ($La_{10}Si_6O_{27}$) obtained from SEM-EDX analysis.

| Element line | Net counts | Weight (%) | Atom (%) | Formula |
|---|---|---|---|---|
| O K | 1034 | 7.87 | 35.02 | O |
| Si K | 2286 | 8.77 | 22.24 | Si |
| La L | 9652 | 83.36 | 42.74 | La |
| La M | 568 | – | – | |
| Total | | 100.00 | 100.00 | |

The intensity of the XRD peaks increases on further heat treatment at 800 °C and maintain the crystalline apatite phase. The average crystallite size is calculated using the Scherer's formula,

$$t = \frac{0.9\lambda}{\beta \cos\theta} \tag{10}$$

where $t$ is average crystallite size, $\lambda$ is the wavelength of Cu-K$\alpha$ radiation, $\beta$ is the full width at half maximum of the diffraction peak and $\theta$ is the Bragg diffraction angle. The $La_{10}Si_6O_{27}$ prepared at 800 °C has an average crystalline size of ~80 nm. Further, transport studies are made on the lanthanum silicate sample obtained at 800 °C.

### 3.4. SEM-EDX analysis

Fig. 4a shows the different magnifications of SEM micrographs of the lanthanum silicate sample, obtained at 800 °C. From Fig. 4a, SEM micrographs showed agglomerated spherical particles of lanthanum silicate and their particle size is ~200 nm. Fig. 4b also shows the energy dispersive spectrum of lanthanum silicate, indicating the existence of O, Si and La in the $La_{10}Si_6O_{27}$ compound. The composition percentage of each element (O, Si and La) of lanthanum silicate obtained from energy dispersive X-ray spectrum is tabulated in Table 1. SEM-EDX results confirm the formation of exact composition of lanthanum silicate. Fig. 5 shows the SEM images taken for the lanthanum silicate pellet sintered at 800 °C and SEM-EDX result confirm the composition of the lanthanum silicate. From Fig. 5, the observed SEM images revealed the formation of agglomerated grains in the lanthanum silicate pellet sintered at 800 °C and the grain size in the sintered lanthanum silicate pellet is found to be ~150 nm. From Fig. 5, the SEM-EDX spectrum confirm the existence of all the O, Si and La element present in the $La_{10}Si_6O_{27}$ pellet sample. The relative density of the sintered pellet is also calculated for $La_{10}Si_6O_{27}$ sample and it is found to be 71%.

### 3.5. Electrical conductivity studies

Fig. 6 shows the impedance plots ($-Z''$ vs $Z'$) obtained at various temperatures for the nanocrystalline $La_{10}Si_6O_{27}$ sample pellet sintered at 800 °C. The measured impedance data of the nanocrystalline lanthanum silicate are analyzed using the winfit software. Fig. 7 shows the typical complex impedance plot (imaginary $-Z''$ vs real $Z'$) obtained at 375 °C. In Fig. 7, the square symbols represent the experimentally observed impedance data and red color continuous line represents their fitted data value. Using the winfit software, the above impedance plot is deconvolated into three depressed semicircles, represented as black color continuous line, along with their respective equivalent circuits. The equation of complex impedance for the equivalent circuit of the three respective depressed semicircles are given by:

$$Z^* = [R_b^{-1} + j\omega C_b]^{-1} + [R_{gb}^{-1} + j\omega C_{gb}]^{-1} + [R_{el}^{-1} + j\omega C_{el}]^{-1} \tag{11}$$

where the subscript b and gb represents the bulk and grain boundary, respectively.

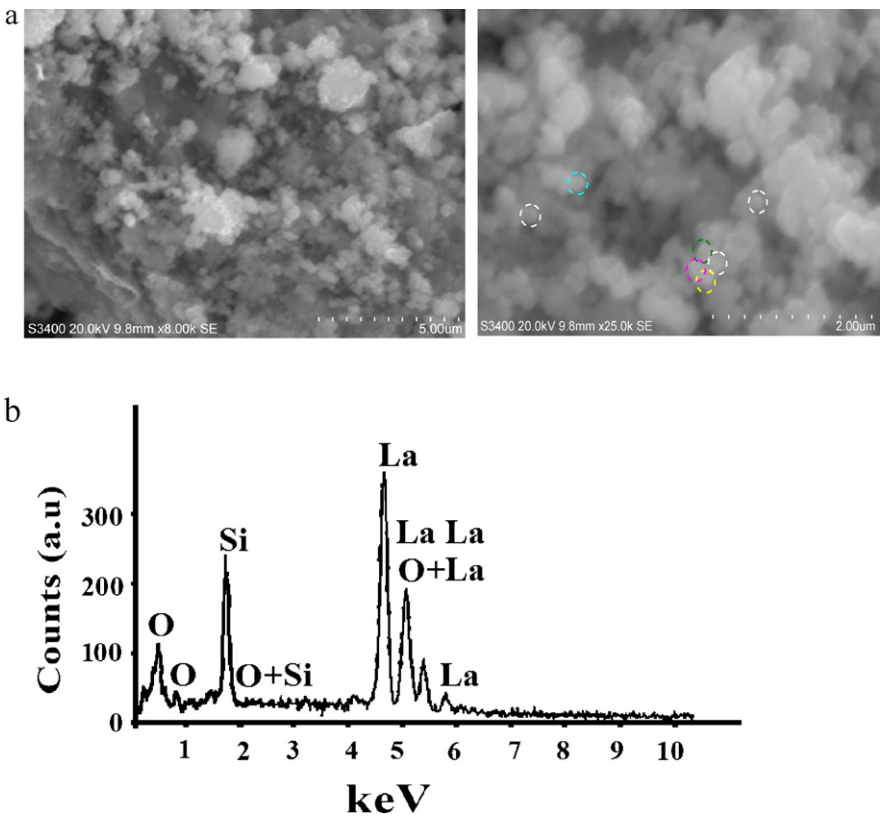


**Fig. 4.** SEM micrograph images and energy dispersive X-ray spectrum (EDX) of the $La_{10}Si_6O_{27}$ sample obtained at 800 °C.

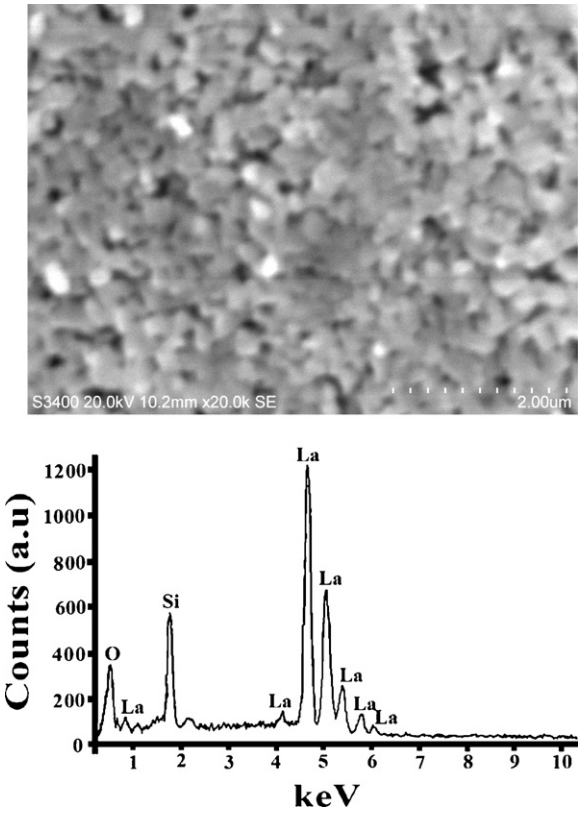


**Fig. 5.** SEM micrograph and SEM-EDX spectrum of $La_{10}Si_6O_{27}$ pellet, sintered at 800 °C.

The bulk (or grain interior) resistance ($R_b$) of $La_{10}Si_6O_{27}$ material is obtained from the intercept of the first depressed semicircle at the real axis in the higher frequency region. The second depressed semicircle is obtained at the middle frequency region corresponds to the grain boundary response of the sintered lanthanum silicate pellet. Third depressed semicircle at the lower frequency region indicates the interfacial effects of the electrode and electrolyte region.

For an ideal solid electrolytes, $Z''_{max}$ and $M''_{max}$ peaks occur at the same frequency and is given by $\omega_{max}\tau = 1$ and the shape of the curve is identical with the dielectric loss predicted by Debye theory [18].

$$Z'' = \frac{R\omega RC}{1+(\omega RC)^2} \quad \text{and} \quad M'' = \frac{C_o}{C}\left(\frac{\omega RC}{1+(\omega RC)^2}\right) \tag{12}$$

From the equations, the term $\omega RC/1+(\omega RC)^2$ in $Z''$ and $M''$ is responsible for the shape of the Debye curve in the frequency plots. Fig. 8 shows $Z''$, $M''$ vs log$f$, obtained at 300 °C for the nanocrystalline $La_{10}Si_6O_{27}$ sample and insert in Fig. 8 also shows that $-Z''$ vs $Z'$ plot of nanocrystalline lanthanum silicate. It can be seen from Fig. 8, that $Z''_{max}$ and $M''_{max}$ do not occur at the same frequency and broadened $Z''$ and $M''$ vs log$f$ spectra are obtained, which is an indication of the wide range distribution of relaxation times. The observed maximum of the semicircle in the middle frequency region for the plot of $-Z''$ vs $Z'$ is matched with the $Z''_{max}$ of the $Z''$ vs freq. plot, shown in Fig. 8 and hence, the peak curve of the $Z''$ vs frequency shows the grain boundary effect, whereas the curve for the $M''$ vs frequency at higher frequency region indicates the grain interior behavior. From the equations $2\pi f_{(Z'')}RC = 1$ at $Z''_{max}$ and $\omega_{(M'')}RC = 1$ at $M''_{max}$ in the $Z''$ and $M''$ vs log$f$ plots, the grain and grain boundary capacitances are calculated using the resistances of grain and grain boundary effects [19]. The calculated values of capacitance and resistances are $C_{gi} = 3.45$ pf and $R_{gi} = 3 \times 10^6\ \Omega$ for grains and $C_{gb} = 40.26$ pf and $R_{gb} = 1.5 \times 10^7\ \Omega$ for grain boundary, as shown in Fig. 8. The capaci-

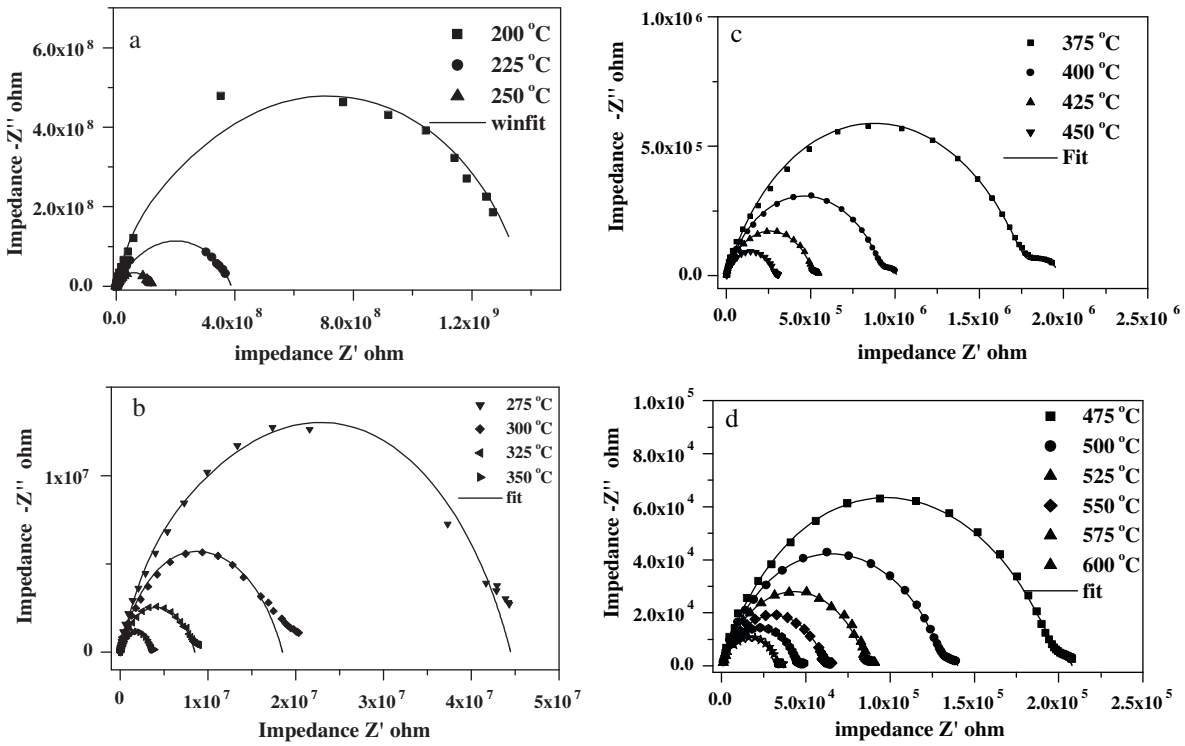


**Fig. 6.** Impedance plots ($Z'$ and $Z''$) obtained at various temperatures for the nanocrystalline $La_{10}Si_6O_{27}$ sample.

tance ratio $C_b:C_{gb} = (\varepsilon_0\varepsilon_r)A/(LC_{gb}) = (\delta_{gb}/d_g)$ is used to calculate the grain boundary thickness of the materials [20,21]. The grain size of the lanthanum silicate sample ~150 nm is measured from the SEM image of the sintered pellet. The grain boundary thickness (<15 nm) is calculated at different temperatures.

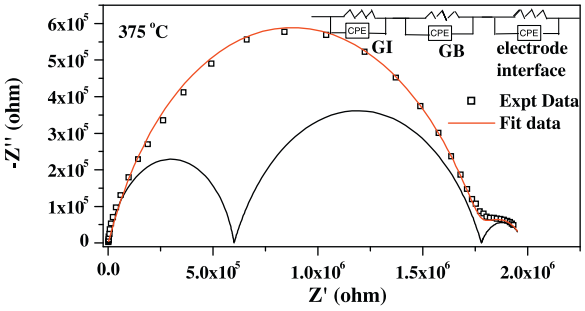


**Fig. 7.** Impedance plot ($-Z''$ vs $Z'$) for nanocrystalline $La_{10}Si_6O_{27}$ sample obtained at 375 °C, fitted using winfit alongwith their corresponding equivalent circuit.

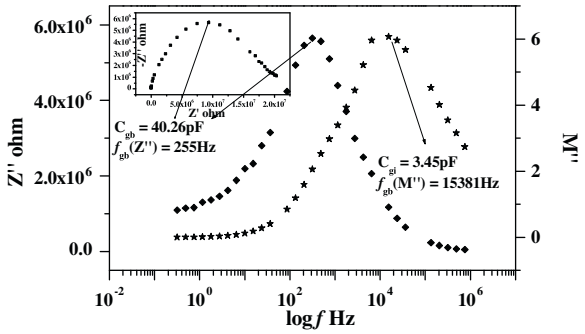


**Fig. 8.** $Z''$, $M''$ vs log$f$ for the nanocrystalline $La_{10}Si_6O_{27}$ sample at 300 °C and inset Fig. $Z''$ vs $Z'$ plot of nanocrystalline lanthanum silicate at 300 °C.

Based on the brick layer model [22,23], the polycrystalline material consists of the grain and grain boundary effects. The bulk conductivity ($\sigma_b$) and grain boundary conductivity ($\sigma_{gb}$) were calculated using the following equations:

$$\sigma_{gi} = \frac{1}{R_{gi}}\frac{ND}{A} = \frac{1}{R_{gi}}\frac{t}{A} \tag{13}$$

$$\sigma_{gb} = \frac{1}{R_{gb}}\frac{N\delta_{gb}}{A} = \frac{1}{R_{gb}}\frac{t}{A}\frac{\delta_{gb}}{D} \tag{14}$$

where $R_{gi}$ and $R_{gb}$ are resistances of bulk (or grain interior) and grain boundary respectively, $t$ is the thickness of the sintered pellet and $A$ is the area of the sintered pellet. $N$ is the number of the grain boundary planes parallel to the electrodes. From the calculated bulk resistance, grain boundary resistance, grain size, grain boundary thickness, the thickness and area of the lanthanum silicate pellet sample, sintered at 800 °C, the grain and grain boundary conductivities are evaluated using the Eqs. (13) and (14). The temperature dependent conductivities are obtained from the analysis of the measured impedance data. Fig. 9 shows the plot of log$\sigma T$ vs $1000/T$ for grain interior and the grain boundary conductivities of the $La_{10}Si_6O_{27}$ sample. At 500 °C, the calculated bulk conductivity of the lanthanum silicate sample is $1.66 \times 10^{-4}$ S cm$^{-1}$. The activation energy is calculated from the slope of the log$\sigma T$ vs $1000/T$ plot and it is found to be 0.94 eV for the bulk conductivity and 1.08 eV for grain boundary conductivity.

The impedance data also provides information on relaxing dipoles of the material in terms of the real and imaginary parts of the complex permittivity:

$$\varepsilon' = \left(\frac{Z''}{Z'^2 + Z''^2}\right)\left(\frac{t}{A\omega\varepsilon_0}\right) \tag{15}$$

$$\varepsilon'' = \left(\frac{Z'}{Z'^2 + Z''^2}\right)\left(\frac{t}{A\omega\varepsilon_0}\right) \tag{16}$$

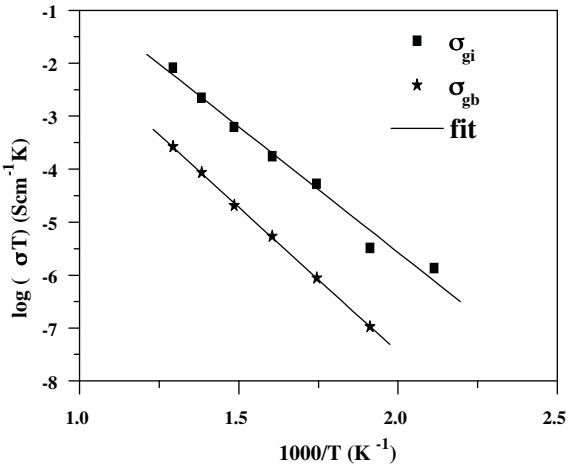


**Fig. 9.** Log $\sigma T$ vs log 1000/$T$ plots for the nanocrystalline $La_{10}Si_6O_{27}$ sample.

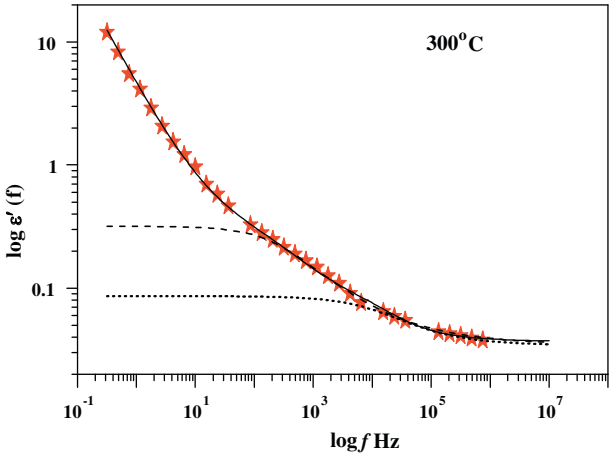


**Fig. 11.** Log $\varepsilon'$ vs log frequency of the nanocrystalline lanthanum silicate, obtained at 300 °C.

The evaluated values of the permittivity ($\varepsilon'$ and $\varepsilon''$) are fitted to the Havriliak and Negami equation using the winfit software. Fig. 10 shows the real permittivity [log $\varepsilon'$] and the imaginary permittivity [log $\varepsilon''$] versus log frequency plots obtained at various temperatures for nanocrystalline lanthanum silicate. Fig. 11, shows the typical permittivity (log $\varepsilon'$ vs log $f$) plot obtained at 300 °C for the lanthanum silicate sample. In Fig. 11, red colour star symbols represent the experimental data of $\varepsilon'$, the continuous line represent the fitted data using Havriliak and Negami equation. The grain interior and grain boundary responses are analyzed from the evaluated permittivity values using winfit software and respectively shown as dotted and dashed lines in Fig. 11. In Fig. 11, three overlapped dispersion regions are observed, which are due to the grain interior, grain boundary and the formation of electrode polarization in the sintered pellet of the lanthanum silicate samples. The observed dispersion in $\varepsilon'$ and $\varepsilon''$ can be explained in terms of the ion diffusion and polarization model. The increase of $\varepsilon'$ towards lower frequencies can be attributed to the contribution from polarisation of charges. In the low frequency region, the ions jump in the field direction and pile up at sites with high free energy barrier in the field direction after successfully hopping sites with low free energy barrier. The piling of charges leads to a net polarisation of the ionic medium. At high frequencies, the periodic reversal of the field takes place so rapidly that there are no excess ion jumps in the field direction, the polarization due to charge pile up at high free energy barrier sites disappears and the observed value of $\varepsilon'$ decreases. The values of dielectric constant $\varepsilon'$ increases and dispersion at $\varepsilon'$ is moving towards the higher frequencies when increasing the temperature of the sintered pellet as shown in Fig. 10. From Fig. 10, dielectric loss $\varepsilon''$ peak curve could not observed in the plot for various temperature. The frequency dependence dielectric loss spectrum implies that the hopping of charge carrier play an important role in their transport processes because a loss peak is an essential feature of the charge carrier hopping transport.

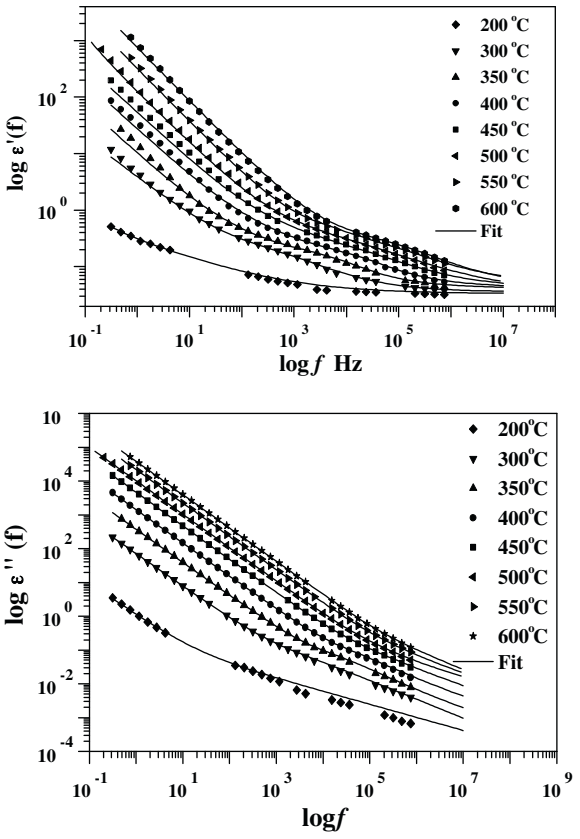


**Fig. 10.** Electric permittivity plots ($\varepsilon'$ and $\varepsilon''$ vs log frequency) obtained at various temperatures for the nanocrystalline $La_{10}Si_6O_{27}$ sample.

The complex electrical Modulus formalism has been used to analyse the electrical properties of the material and the complex electric modulus can be represented by the following expression:

$$M^* = M' + iM'' = \frac{1}{\varepsilon^*} \quad (17)$$

In Fig. 12, the symbols correspond to the experimental data and the line represents the fit of $M'$ and $M''$ to different frequencies for various temperature. From Fig. 12, at lower frequency, $M'$ value is nearly zero and it rises while increasing the frequency and saturates ($M_\infty$) at higher frequencies. The dispersion region of $M'$ moves towards the higher frequencies as the temperature increases. The shape of observed two overlapped $M''$ peak curve exhibits as an asymmetric and the maximum of the $M''$ ($M''_{max}$) are not centered at their dispersion regions of $M'$ in the measured frequency window, which are indicated as non Debye behaviour. The $M''_{max}$ value is remains constant and it shifts towards the higher frequency while increasing the temperature. Fig. 13 shows the electric modulus plot dependence on the frequencies for nanocrystalline lanthanum silicate samples, obtained at 300 °C. Continuous lines in green colour represent the simulated response for the grain boundary behavior and the continuous lines in blue colour represent the simulated response for the grain interior behavior of the lanthanum silicate sample. From the $M''$ vs log $f$ plot, the value of the relaxation time

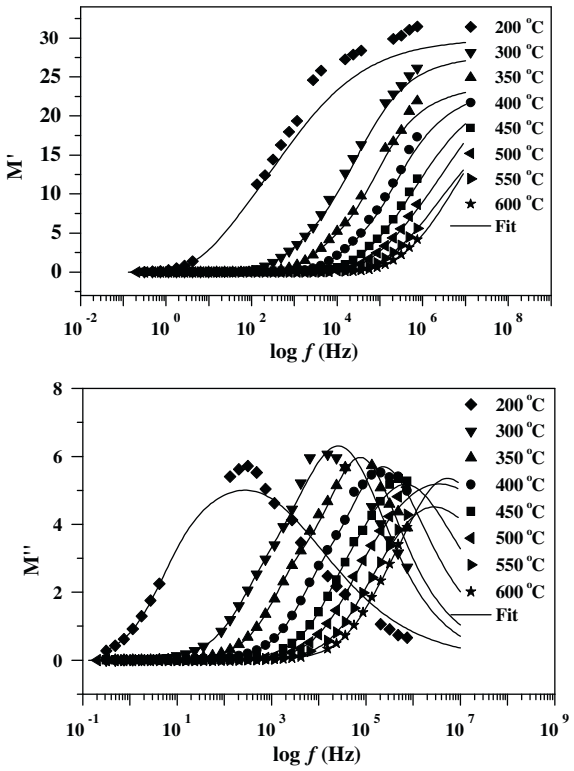


**Fig. 12.** Modulus plots ($M'$ and $M''$ vs log frequency) obtained at various temperatures for the nanocrystalline $La_{10}Si_6O_{27}$ sample.

($\tau$) is observed from the frequency ($f_{max}$) for the grain interior and the grain boundary of the lanthanum silicate pellet. The relaxation time $\tau$ follows the Arrhenius equation [24]:

$$\tau = \tau_0 \exp\left(\frac{-E\tau}{KT}\right), \quad (18)$$

where $\tau_0 = 2\pi f_{max}$.Fig. 14 shows the log $\tau$ vs 1000/$T$ plot for nanocrystalline lanthanum silicate sample at different temperatures. The log $\tau$ vs 1000/$T$ is fitted to Arrhenius Eq. (18) using the linear least square fit and slope gives the relaxation activation energy $E_\tau$. The activation energies $E_a$ and $E_\tau$ are given in Table 2 for nanocrystalline lanthanum silicate sample. The activation energy $E_{dc}$ is slightly higher than the activation energy $E_\tau$, in order to create the defects in the grain interior and the grain boundary of the

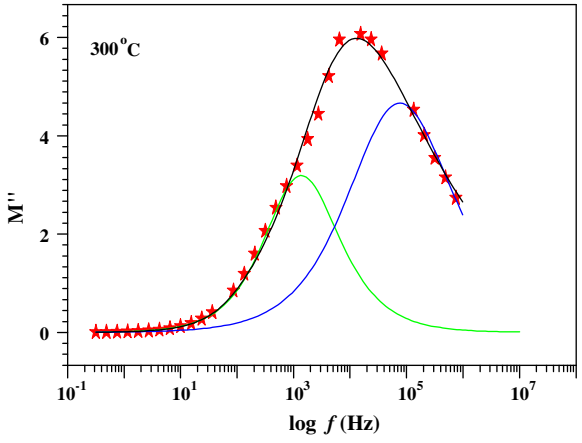


**Fig. 13.** $M''$ vs log $f$ plot for nanocrystalline lanthanum silicate samples, obtained at 300 °C.

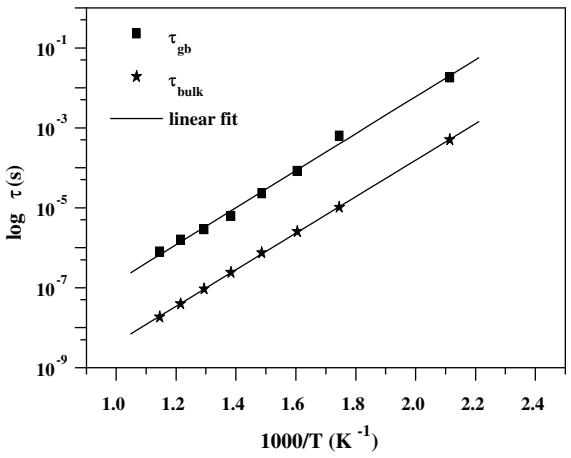


**Fig. 14.** Log $\tau$ vs log 1000/$T$ plots for the nanocrystalline $La_{10}Si_6O_{27}$ sample.

**Table 2**
Activation energies, resistances, capacitances and size of grain interior and grain boundary for lanthanum silicate sintered pellet at 800 °C.

| | Grain interior | Grain boundary |
|---|---|---|
| Activation energy (dc) | 0.94 eV | 1.08 eV |
| Activation energy ($\tau$) | 0.906 | 0.917 |
| Resistance ($R$) at 300 °C | 3e6 | 1.55e7 |
| Capacitance ($C$) at 300 °C | 3.45 pF | 40.2 pF |
| Size | ~150 nm (grain size) | <20 nm (grain boundary size) |

nanocrystalline lanthanum silicate sample. Since the charge carrier concentration is low, the calculated activation energies $E_{dc}$ and $E_\tau$ are higher in the grain boundary and the conductivity is also lower than the grain interior of the lanthanum silicate.

## 4. Conclusions

Nanocrystalline lanthanum silicate $La_{10}Si_6O_{27}$ material was synthesized by sol–gel method. TG/DTA curves predicted the thermal behavior of the material and confirmed the presence of organic residuals with adsorbed water, which are removed on heating. FTIR spectra confirmed the formation of $SiO_4$ and La–O network in the lanthanum silicate samples at high temperature. The XRD patterns confirmed the formation of pure crystalline apatite $La_{10}Si_6O_{27}$ phase and its average crystallite size is found to be 80 nm. SEM micrographs showed agglomerated spherical particles of lanthanum silicate and their particle size is ~200 nm. Also, SEM-EDX results confirm the formation of exact composition of lanthanum silicate. The grain interior and the grain boundary conductivities are evaluated by analyzing the measured impedance data of $La_{10}Si_6O_{27}$ sample using the brick layer model. The relaxation behavior of the grain interior and grain boundary of the nanocrystalline lanthanum silicate are also obtained from the analyzed electrical permittivity and electrical modulus data fitted to Havriliak and Negami function using win fit software.

## Acknowledgements

NS gratefully acknowledge DRDO, DST, CSIR, AICTE and UGC, Govt of India, for receiving financial support in the form of major research projects. NN acknowledges the CSIR [CSIR: 9/559/(0054)/2008/EMR-I], Government of India, for the award of senior research fellowship. Authors would like to thank Central Instrumentation Facility (CIF), Pondicherry University for using TG/DTA, FTIR and SEM facilities for the present work.

## References


[1] S.C. Singhal, Solid State Ionics 135 (2000) 305.
[2] M. Winter, R.J. Brodd, Chem. Rev. 105 (3) (2005) 1021.
[3] H. Yokokawa, N. Sakaki, T. Sahorita, K. Yamaji, Fuel Cells 1 (2001) 117.
[4] F. Nishiwaki, T. Inagaki, J. Kano, J. Akikusu, N. Murakam, K. Hosoi, J. Power Sources 157 (2006) 809.
[5] V.V. Kharton, F.M.B. Marques, A. Atkinson, Solid State Ionics 174 (2004) 135.
[6] Laura León-Reina, E.R. Losilla, Maria Martinez-Lara, Sebastián Bruque, Anna Llobet, D.V. Sheptyakov, M.A.G. Aranda, J. Mater. Chem. 15 (2005) 2489.
[7] E.J. Abram, D.C. Sinclair, A.R. West, J. Mater. Chem. 11 (2001) 1978.
[8] U. brassmann, G. Knoner, H.E. Schaefer, R. Wurschum, Rev. Adv. Mater. Sci. 6 (2004) 7.
[9] H. Schimt, J. Non-Cryst. Solids 100 (1988) 51.
[10] C.J. Brinker, G.W. Scherer, Sol–Gel Science: The Physics and Chemistry of Sol–Gel Processing, Academic Press, New York, 1990.
[11] I. Prakash, P. Muralidharan, N. Nallamuthu, M. Venkateswarlu, D. Carnahan, N. Satyanarayana, J. Am. Ceram. Soc. 89 (7) (2006) 2220.
[12] N. Nallamuthu, I. Prakash, M. Venkateshwarlu, S. Balasubramaniyam, N. Satay-narayana, Mater. Chem. Phys. 111 (1) (2008) 24.
[13] J.R. MacDonald, Impedance Spectroscopy, Wiley, New York, 1987.
[14] S. Havriliak, S. Negami, Polymer 8 (1967) 161.
[15] S. Havriliak, S. Negami, Polymer 10 (1969) 859.
[16] Socrates George, Infra red and Raman Chracteristic Group Frequencies Tables and Charts, 3rd ed., John Wiley & Sons, England, 2001.
[17] T. Kharlamova, S. Pavlova, V. Sadykov, M. Chaikina, T. Krieger, O. Lapina, D. Khabibulin, A. Ishchenko, V. Zaikovskii, C. Argirusis, J. Frade, Eur. J. Inorg. Chem. 6 (2008) 939–947.
[18] A.R. West, D.C. Sinclair, Naohiro Hirose, J. Electroceram. 1 (1997) 65.
[19] C. Tian, Siu-Wai Chan, Solid State Ionics 134 (2000) 89.
[20] J.C.C. Abrantes, J.A. Labrincha, J.R. Frade, J. Eur. Ceram. Soc. 20 (2000) 1603.
[21] G.M. Christie, F.P.F. Van Berkel, Solid State Ionics 83 (1996) 17.
[22] J. Fleig, J. Maier, J. Am. Ceram. Soc. 82 (12) (2000) 34.
[23] X. Guo, W. Sigle, J. Maier, J. Am. Ceram. Soc. 86 (2003) 77.
[24] P. Muralidharan, M. Venkateswarlu, N. Satyanarayana, Solid State Ionics 166 (2004) 27.